Chemical Physics Letters 772 (2021) 138547

Contents lists available at ScienceDirect

Chemical Physics Letters

journal homepage: www.elsevier.com/locate/cplett

Research paper

Structural and optical behavior of nano-scaled luminous green-emitting $Ca_9Y(PO_4)_7:Tb^{3+}$ phosphor for competent lighting devices

Anju Siwach, Dinesh Kumar *

Department of Chemistry, Deenbandhu Chhotu Ram University of Science & Technology, Murthal, Sonepat 131039, India

ARTICLE INFO

Keywords:
Solution-combustion
Rietveld study
Space symmetry
Band-gap
CIE chromaticity co-ordinates
Quantum efficiency

ABSTRACT

Nano-sized $Ca_9Y_{(1-x)}(PO_4)_7:xTb^{3+}$ phosphor series was synthesized via solution-combustion method for the first time. Rietveld study revealed the incorporation of Tb^{3+} ions into monoclinic host lattice of R3*c*(161) space symmetry. The diffuse reflectance spectral investigations depicted the lowering of band-gap (E_g) value from 4.44 to 4.27 eV for $Ca_9Y(PO_4)_7$ and $Ca_9Y_{0.30}Tb_{0.70}(PO_4)_7$, respectively. Under near-Ultraviolet excitation, PL spectra yielded luminous green emission at 544 nm ($^5D_4 \rightarrow {}^7F_5$). For $Ca_9Y_{0.30}Tb_{0.70}(PO_4)_7$ system, quantum efficiency and CIE chromaticity coordinates were determined to be 96% and (0.252, 0.564), respectively. The results as-obtained predict the potential implications of $Ca_9Y_{0.30}Tb_{0.70}(PO_4)_7$ nanophosphor as primary green component in WLEDs.

1. Introduction

In the blooming era of nanoscience and nanotechnology, rare-earth metal ions activated luminescent nanophosphors have offered substantial input at the level of materials chemistry and physics owing to their wide array of utilities in laser, sensors, detectors, solar collectors, lighting devices, display panels, etc. [1,2]. Phosphor converted white light-emitting diodes (PC-WLEDs) that are also regarded as a source of 4th generation solid-state lighting [3], have completely replaced the conventional lighting devices like incandescent bulbs and fluorescent lamps [4,5]. Besides that, no wonder to say that WLEDs are becoming a more and more significant component of conserving energy worldwide as they produce excellent luminescence at very low power consumption and are environmentally friendly causing no pollution in nature [6–9]. Consequently, they can minimize the global power needs as well as the use of depleting fossil fuels [10].

In recent times, owing to the greater stability and outstanding photoluminescent (PL) attributes, the light-emitting nanophosphor substances have evolved as a core contributor to innovative illuminating devices [11]. In order to synthesize such luminescent nanomaterials, some suitable and appropriate dopant ions (usually trivalent rare-earth ions) are incorporated into the host inorganic matrix, and consequently, dopant ions act as a key point to obtain desired and enhanced PL properties [12]. For our present research work, we have selected Tb^{3+} ion as a dopant ion which is believed to be the most significant dopant among trivalent rare-earth ions as it provides a strong sparkling green-emission under ultraviolet (UV) or near-ultraviolet (NUV) excitation range [11]. Likewise, the selection of some pertinent inorganic host crystal lattice is just as important as the choice of dopant ion. The inorganic host materials of type $Ca_9R(PO_4)_7$ (here, R is trivalent rare-earth ion metals i.e. Gd, Y, La) have gained high limelight in the domain of luminescent nanomaterials by virtue of their wide range of benefits such as high band-gap value, greater thermal and chemical stability, persistent luminescence in the visible region, unaltered crystal lattice upon doping with rare-earth ion, and availability of many cationic sites [13–16]. In compliance with this, we have opted $Ca_9Y(PO_4)_7$ host system to dope with Tb^{3+} ion for our current study.

From the literature survey, only one study containing Tb^{3+} and Eu^{3+}-Tb^{3+} ions co-doped $Ca_9Y(PO_4)_7$ phosphors has been reported that described the attempt to synthesize a very weak green-emitting singly doped $Ca_9Y(PO_4)_7:Tb^{3+}$ system. Hence, the requirement of co-doping was given preference to strengthen the optical properties of as-synthesized nanophosphors. So far, various research articles regarding $Ca_9Y(PO_4)_7:Eu^{3+}$ by Dahiya and co-workers [17]; $Ca_9Y(PO_4)_7:Sm^{3+}$ by Huang and co-workers [3]; $Ca_9Y(PO_4)_7:Eu^{2+}$, Mn^{2+} by Huang and co-workers [18], also by H. Zhang and co-workers [14]; $Ca_9Y(PO_4)_7$:Eu^{2+}-Tb^{3+} by Tang and co-workers [19]; $Ca_9Y(PO_4)_7:Yb^{3+}/Er^{3+}/Tm^{3+}$ by Du and co-workers [20]; $Ca_9Y(PO_4)_7:Eu^{2+}$, Yb^{3+} by Sun and co-workers [21]; $Ca_9Y(PO_4)_7:Tm^{3+}$, Dy^{3+} by Wu and co-workers [15], and $Ca_9Y(PO_4)_7$: Ce^{3+}, Mn^{2+} by Huang and co-workers [22] have been

* Corresponding author.
E-mail address: dineshdalal8@rediffmail.com (D. Kumar).

https://doi.org/10.1016/j.cplett.2021.138547
Received 14 December 2020; Received in revised form 20 February 2021; Accepted 11 March 2021
Available online 22 March 2021

reported. Usually, host matrices of such type have been fabricated using a high-temperature solid-state route of synthesis. But no study on successful solution combustion synthesis of full series of single Tb^{3+} ion-doped $Ca_9Y(PO_4)_7$ nanophosphors have been reported.

In our current research study, we are reporting the fabrication of a series of green-emitting $Ca_9Y_{(1-x)}Tb_x(PO_4)_7$ (x = 0.10–0.90 mol) crystalline nanophosphors which were synthesized the first time via a simple yet economic and effective urea-assisted solution combustion route at 1200 °C inside the muffle furnace in just 3 h. This route has led to the increased PL properties of $Ca_9Y_{(1-x)}Tb_x(PO_4)_7$ nanophosphor samples. Upon doping with Tb^{3+} ions $Ca_9Y(PO_4)_7$ bestows fine green emission at 544 nm due to $^5D_4 \rightarrow {}^7F_5$ transition [1]. In addition to the transmission electron micrograph of $Ca_9Y_{0.30}Tb_{0.70}(PO_4)_7$ nanophosphor, Williamson-Hall (W-H) equation was employed on the $Ca_9Y_{(1-x)}Tb_x(PO_4)_7$ nanophosphors for the first time to evaluate the grain size and dislocation density of all the samples of the series. Rietveld refinement using GSAS (General Structure Analysis System) software to examine crystal lattice structure and unit cell dimensions of $Ca_9Y_{0.30}Tb_{0.70}(PO_4)_7$ nanophosphor system is also done. The energy band-gap (in eV) evaluation of $Ca_9Y(PO_4)_7$ host and $Ca_9Y_{0.30}Tb_{0.70}(PO_4)_7$ nanophosphor sample was carried out using diffuse reflectance (DR) analysis. The PL properties including excitation and emission peaks, concentration quenching, and energy transfer mechanism have been thoroughly investigated. The fluorescence decay profile of all the samples of $Ca_9Y_{(1-x)}Tb_x(PO_4)_7$ nanophosphor series is also discussed. The radiative lifetime is calculated using Auzel's fitting function. Consequently, non-radiative rates (s^{-1}) as well as internal quantum efficiencies (IQE) for $Ca_9Y_{(1-x)}Tb_x(PO_4)_7$ (x = 0.10–0.90 mol) crystalline nanophosphor samples are assessed. Moreover, the Commission Internationale de'Eclairage (CIE) color co-ordinates of the as-synthesized series of samples are characterized.

These complete research evaluations have not been reported before. Our findings have revealed that under near-UV excitation $Ca_9Y(PO_4)_7$:Tb^{3+} nanophosphor showed a strong green emission which might have potential implications in lighting sources and devices.

2. Experimental section

2.1. Materials and synthesis

A highly efficient and time-savvy solution combustion route was employed to synthesize a series of $Ca_9Y_{(1-x)}Tb_x(PO_4)_7$ (x = 0, 0.10–0.90 mol) powdered crystalline samples. For the synthesis process, calculated amounts of highly pure starting materials involving metal nitrates such as $Ca(NO_3)_2{\cdot}4H_2O$, $Y(NO_3)_3{\cdot}6H_2O$, $Tb(NO_3)_3{\cdot}6H_2O$, $(NH_4)_2HPO_4$, and organic fuel (urea) were used without performing further purification. All the precursors were dissolved in the least amount of double distilled water taken in a pyrex beaker in order to get a saturated solution. Then, the beaker containing the solution was initially put on a hot plate (100 °C) which was heated for 5–10 min, and lastly, it was transferred into a muffle furnace maintained at 500 °C for about 15–20 min. The occurrence of highly exothermic, self-prevailing ultra-fast chemical reaction inside the furnace led to the formation of white dry crystalline solid. The same operation was adopted to synthesize differently doped phosphor samples of the series. The dried solid products were collected from the furnace, cooled to room temperature, crushed into the fine powdered form using agate mortar-pestle, and finally, these were put into alumina crucibles for sintering at 1200 °C inside the furnace to obtain $Ca_9Y_{(1-x)}Tb_x(PO_4)_7$ (x = 0, 0.10–0.90 mol) nanophosphors exhibiting utmost luminescence characteristics. A combined chemical combustion reaction occurring inside the furnace for $Ca_9Y_{0.30}Tb_{0.70}(PO_4)_7$ nanophosphor sample may be represented as follows:

$$30Ca(NO_3)_2{\cdot}4H_2O + Y(NO_3)_3{\cdot}6H_2O + 2.333\ Tb(NO_3)_3{\cdot}6H_2O + 23.333\ (NH_4)_2HPO_4 + 350NH_2.CO.NH_2 \rightarrow 3.333Ca_9Y_{0.30}Tb_{0.70}(PO_4)_7 + 408.333\ N_2 + 945H_2 + 350CO_2$$

2.2. Spectral measurements

To check the phase purity of as-obtained $Ca_9Y_{(1-x)}Tb_x(PO_4)_7$ (x = 0, 0.10–0.90 mol) nanophosphors, PXRD (powder X-ray diffraction) data were collected using "Rigaku Ultima-IV X-ray diffractometer" fitted with Cu Kα radiation source. The diffractometer was operated in 2θ ranging from 10° to 80° with a scan speed of 1°/min. Rietveld structural refinement of $Ca_9Y_{0.30}Tb_{0.70}(PO_4)_7$ crystalline sample was performed using "GSAS (General Structure Analysis System) program [23,24] and further the particle size and surface morphology of same crystalline sample was determined via "JeoI JSM-6510 Scanning Electron Microscope (SEM)" and "Technai-G^2 Transmission Electron Microscopy (TEM)". Additionally, the energy band-gap values were determined with the help of diffuse reflectance spectral studies and the spectral data was obtained from "Shimadzu UV-3600 plus spectrophotometer" Equipped with an integrating sphere, and $BaSO_4$ was taken as a reference standard. The room temperature photoluminescence excitation (PLE), PL emission, and fluorescence decay curves were recorded on "Hitachi F-7000 Fluorescence Spectrophotometer". The Commission Internationale de I'Eclairage (CIE) chromaticity co-ordinates were derived using PL emission spectral data of the samples in MATLAB software [25].

3. Results and discussion

3.1. Crystalline structure and morphological investigation

The powdered XRD patterns of pure $Ca_9Y(PO_4)_7$ host (CYPO) and differently doped $Ca_9Y_{(1-x)}Tb_x(PO_4)_7$ (x = 0.10–0.90 mol) phosphor samples are displayed in Fig. 1. All the X-ray diffractogram peaks of various samples are ascertained to be systematic and consistent with that of standard JCPDS data (Card No. 046–0402). This further indicates the chemical and phase purity of as-synthesized CYPT i.e. $Ca_9Y_{(1-x)}Tb_x(PO_4)_7$ (x = 0, 0.10–0.90 mol) samples and activation of Tb^{3+} ions in CYPO host crystallizes in a single phased lattice. However, a slight regular shift in the peak position towards the right-hand side is observed in Tb^{3+} ions doped CYPT nanophosphors which is shown parallelly in Fig. 1. This might be due to the smaller ionic size of dopant (Tb^{3+}) ion which is replacing the rare-earth metal (Y^{3+}) ion of greater size from the host CYPO lattice.

To gain insight into the crystal structure of CYPT nanophosphors, Rietveld refinement using GSAS software was performed on XRD data of $Ca_9Y_{0.30}Tb_{0.70}(PO_4)_7$ nanophosphor which gave a well-fitted refinement structure with reduced fitted parameters χ^2 = 1.96, R_p = 12.4%, and R_{wp} = 17.2%. The as-obtained calculated, observed, diffraction profile, Bragg's reflection, and the difference between observed and calculated parameters are represented clearly in Fig. 2. Using DIAMOND software, the crystalline structure of $Ca_9Y_{0.30}Tb_{0.70}(PO_4)_7$ nanophosphor was derived as an outcome of Rietveld refinement analysis and from the previous research reports, it is evident that the CYPO matrix provides three octa-coordinated, non-centrosymmetric crystalline sites for metal and dopant ion, and one hexa-coordinated centrosymmetric site for Ca^{2+} ions only. The crystal structure analysis of our $Ca_9Y_{0.30}Tb_{0.70}(PO_4)_7$ system also confirms the occurrence of a total of 4 crystalline sites, 3 are Ca_1/Y/Tb, Ca_2/Y/Tb, Ca_3/Y/Tb (all octa co-ordinated), and the fourth one is represented by Ca_4 (Hexa co-ordinated site) which are depicted well in Fig. 3. Table 1 reflects the comparison of various crystal parameters like unit cell dimensions, shape, volume, density, space group, etc. of both host CYPO matrix and $Ca_9Y_{0.30}Tb_{0.70}(PO_4)_7$ nanophosphors while the Table 2 is depicting the refined occupancy data for nanocrystalline $Ca_9Y_{0.30}Tb_{0.70}(PO_4)_7$ phosphor.

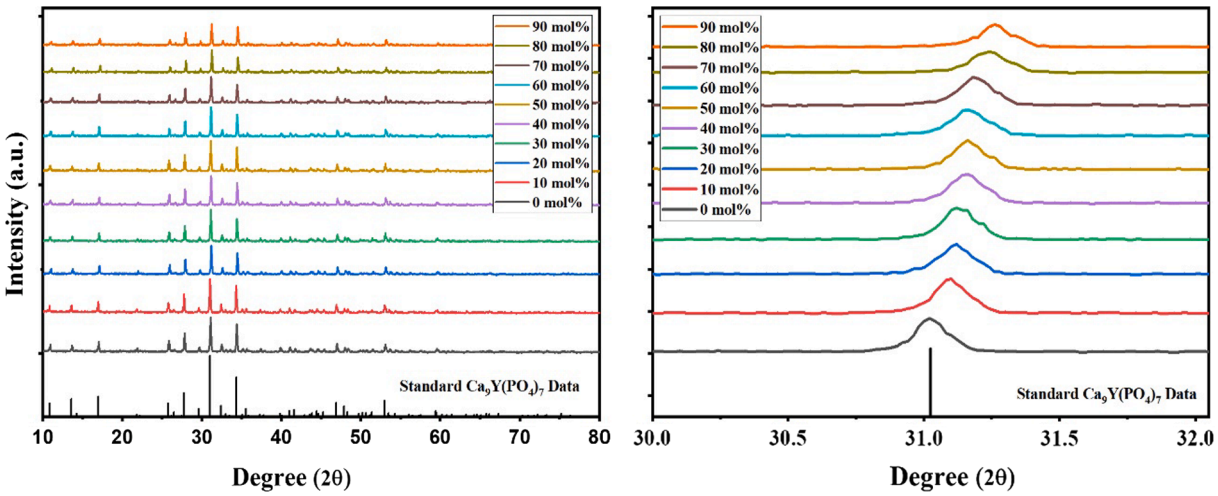

Fig. 1. X-ray diffraction pattern of $Ca_9Y_{(1-x)}Tb_x(PO_4)_7$ nanophosphors (x = 0, 0.10–0.90 mol) along with the standard data of host matrix. A regular peak shift as-observed due to the addition of dopant Tb^{3+} ions with different concentration in the host matrix is shown along with X-ray diffractograms.

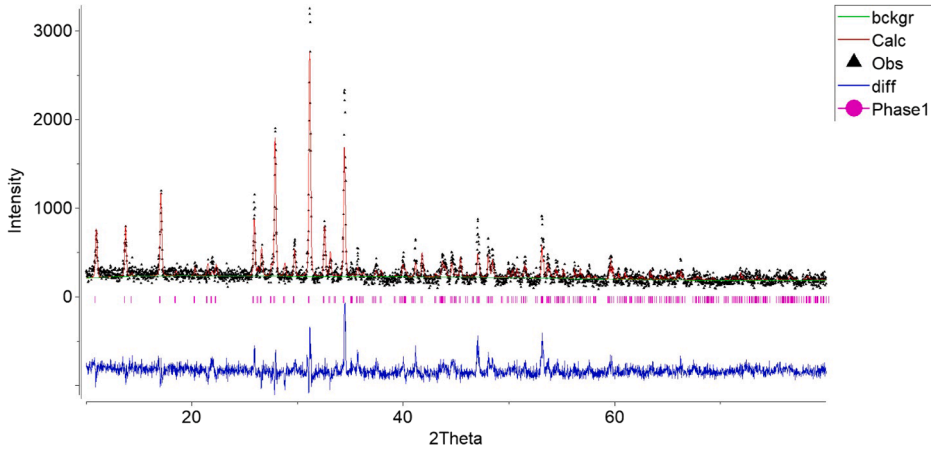

Fig. 2. Rietveld refinement pattern for the XRD data of $Ca_9Y_{0.30}Tb_{0.70}(PO_4)_7$ nanophosphor sample having reduced fitted parameters $\chi^2 = 1.96$, $R_p = 12.4\%$, and $R_{wp} = 17.2\%$.

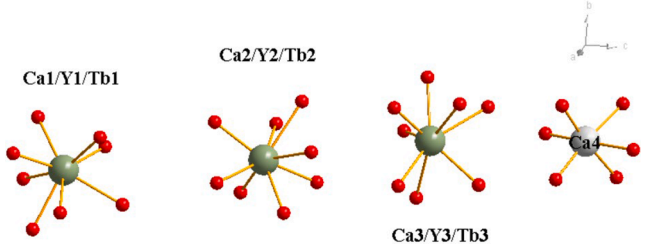

Fig. 3. Unit cell view of $Ca_9Y_{0.30}Tb_{0.70}(PO_4)_7$ nanophosphor sample showing the co-ordination environment around different cations.

All the while, the value of radius % difference (D_r) is also calculated by utilizing the equation given below [26,27]:

$$D_r = \frac{R_m(CN) - R_d(CN)}{R_m(CN)} \times 100\% \quad (1)$$

where, the radius of the host metal ion and dopant ion is represented by R_m (Y^{3+}) and R_d (Tb^{3+}) respectively, and CN shows the co-ordination number of a metal ion. Using the above equation, the value of D_r is calculated to be ≈ 8% which is quite admissible as it has come out to be less than 30%. Hence, it becomes evident from the result obtained so far that the entrance of dopant Tb^{3+} ions in CYPO has not affected its structural prototype in any way.

Table 1
Comparison of crystal structure data of $Ca_9Y_{0.30}Tb_{0.70}(PO_4)_7$ nanophosphor with standard $Ca_9Y(PO_4)_7$.

Formula	$Ca_9Y(PO_4)_7$	$Ca_9Y_{0.30}Tb_{0.70}(PO_4)_7$
Formula Weight	1114.39	1162.45
Crystal shape	Trigonal	Trigonal
Space Group	R3*c*(1 6 1)	R3*c*(1 6 1)
a (Å)	10.4470	10.4453(12)
b (Å)	10.4470	10.4453(12)
c (Å)	37.320	37.319(7)
$\alpha = \beta = \gamma$ (degree)	90	90
Volume (Å^3)	3527.41	3515.04
Z	6	6
Density (g/cm^3)	3.147	3.281

In a way to examine the crystallite sizes and morphologies of Tb^{3+} doped CYPO sample, different equation and instrumental techniques like SEM and TEM are utilized. Firstly, Scherrer equation is employed to determine the average crystallite size (D) of the whole series of $Ca_9Y_{(1-x)}Tb_x(PO_4)_7$ (x = 0.10–0.90 mol) phosphors which is mentioned below [1,28–30]:

Table 2
Refined occupancy data for nanocrystalline $Ca_9Y_{0.30}Tb_{0.70}(PO_4)_7$ phosphor.

Atom	Wyck.	Site	S.O.F.	x/a	y/b	z/c	U [Å^2]
O1	18b	1		0.00270	0.27930	0.10900	0.2500
O2	18b	1		0.07630	0.42470	0.01940	0.2500
O3	18b	1		0.09400	0.17600	0.26840	0.2500
O4	18b	1		0.13300	0.15000	0.48670	0.2500
Ca1	18b	1	0.89	0.14800	0.27500	0.05580	0.2500
Y1	18b	1	0.033	0.14800	0.27500	0.05580	0.2500
Ca2	18b	1	0.89	0.14800	0.28100	0.16240	0.2500
Y2	18b	1	0.033	0.14800	0.28100	0.16240	0.2500
O5	18b	1		0.17570	0.08130	0.19720	0.2500
O6	18b	1		0.24470	0.21830	0.11440	0.2500
Ca3	18b	1	0.89	0.28870	0.13130	0.29510	0.2500
Y3	18b	1	0.033	0.28870	0.13130	0.29510	0.2500
O7	18b	1		0.28870	0.14230	0.05430	0.2500
P1	18b	1		0.32270	0.13930	0.09480	0.2500
P2	18b	1		0.35070	0.16430	0.19910	0.2500
O8	18b	1		0.38870	0.05030	0.17680	0.2500
O9	18b	1		0.39570	0.14930	0.23730	0.2500
P3	6a	3.		0	0	0	0.2500
O10	6a	3.		0	0	0.0435	0.2500
Ca4	6a	3.		0	0	0.2287	0.2500
Tb1	18b	1	0.077	0.14800	0.27500	0.05580	0.0250
Tb2	18b	1	0.077	0.14800	0.28100	0.16240	0.0250
Tb3	18b	1	0.077	0.28870	0.13130	0.29510	0.0250

$$D = \frac{K.\lambda}{\beta\cos\theta} \tag{2}$$

where K is the shape factor constant which equals 0.941, λ shows wavelength of X-ray radiations used, θ be the diffraction angle, and β represents the full width half maxima (FWHM) value of the sample in radian. The results obtained from Scherrer equation depict that the average crystallite sizes of CYPT phosphor samples lie in the range of 40–60 nm. In addition to that, effective particle sizes (D) and effective value of microstrain (ε) of all the samples of CYPT series assessed utilizing Williamson-Hall (W-H) equation given as follows [17,30,31]:

$$\beta\cos\theta = 4\varepsilon\sin\theta + \frac{K.\lambda}{D} \tag{3}$$

Using the W-H equation, a plot name W-H plot is drawn for$\beta\cos\theta$ (Y-axis) vs 4sinθ (X-axis) for the differently doped concentration of Tb^{3+} ions in CYPT samples which is shown in Fig. 4. The intercept value of each plot is equivalent to $\frac{K\lambda}{D}$ part of the W-H equation gives the value of D i.e. effective particle sizes (nm) for each concentration in the CYPT series. For powdered crystalline $Ca_9Y_{(1-x)}Tb_x(PO_4)_7$ (x = 0.10–0.90 mol) samples, average crystallite sizes as per Scherrer equation and W-H equation along with dislocation density (δ) of all nanophosphors are summarized in Table 3. Figs. 5 and 6 illustrates the typical SEM and TEM image of single-phase $Ca_9Y_{0.30}Tb_{0.70}(PO_4)_7$ crystalline nanophosphor system, respectively and it clearly shows the occurrence of more or less spherical shaped agglomerated particles of nano-range 40–60 nm, which is in good agreement with the results estimated from Scherrer equation and W-H plot.

In a way to evaluate the magnitude of optical band-gap (E_g) value of $Ca_9Y(PO_4)_7$ and $Ca_9Y_{0.30}Tb_{0.70}(PO_4)_7$ nanophosphor samples, Kubelka-Munk (K-M) function is used to transform observed reflectance data of both nanophosphors into the absorption spectral form. Hence, the energy band-gap value (E_g) in eV can be calculated by using a main relation and is shown below [2,16,32]:

$$[F(R_\infty)h\nu]^n = C(h\nu - E_g) \tag{4}$$

This equation was given by Tauc, Davis, and Mott [11] in which $h\nu$ is photon energy, C denotes constant of proportionality, and value of n is 0.5 and 2 for indirect allowed and direct allowed transitions, respectively. $F(R_\infty)$ refers to the K-M function which is defined by the following expression [23,32,33]:

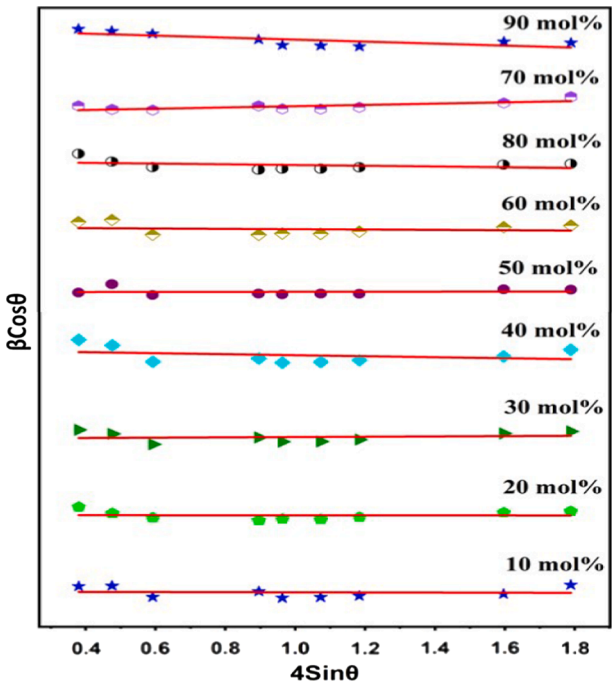

Fig. 4. W-H plot of $Ca_9Y_{(1-x)}Tb_x(PO_4)_7$ (x = 0.10–0.90 mol) phosphor samples showing variation of βCosθ (Y-axis) with 4Sinθ taken on X-axis.

Table 3
Crystallite size (nm) and dislocation density (δ) of various crystalline samples of $Ca_9Y_{(1-x)}Tb_x(PO_4)_7$ phosphors (x = 0.10–0.90 mol).

S. No.	Tb^{3+} concentrations (mol%)	Crystallite size (nm) by Scherrer Formula	Crystallite size (nm) by W-H Plot	Dislocation Density, δ ($\times10^{-4}$)
1	10	50.91	43.60	3.858
2	20	51.18	45.76	3.817
3	30	51.97	47.97	3.702
4	40	50.57	37.99	3.909
5	50	49.54	47.01	4.073
6	60	53.34	44.36	3.514
7	70	51.88	58.51	3.715
8	80	47.27	39.27	4.474
9	90	48.99	40.43	4.166

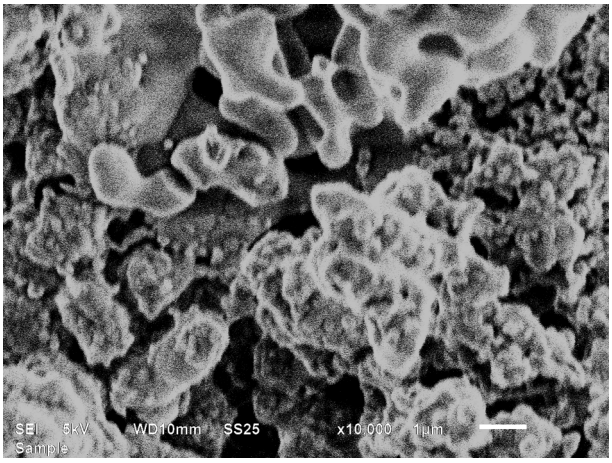

Fig. 5. SEM image of $Ca_9Y_{0.30}(PO_4)_7$:0.70 Tb^{3+} crystalline powder calcined at 1200 °C.

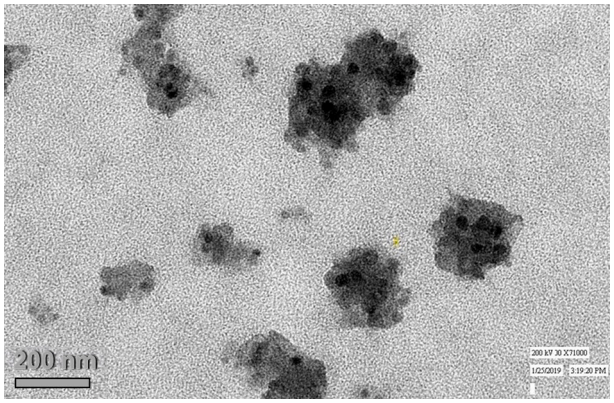

Fig. 6. A typical TEM picture of the crystalline $Ca_9Y_{0.30}(PO_4)_7$:0.70 Tb^{3+} phosphor sample.

$$F(R_\infty) = \frac{(1-R_\infty)^2}{2R_\infty} = \frac{K}{S} \quad (5)$$

Here, K-M function $[F(R_\infty)]$ signifies the ratio of absorption coefficient (K) and scattering coefficient (S), and R_∞ is the ratio of reflectivity of the sample to the reflectivity of standard reference. Fig. 7 represents a plot of $[F(R_\infty)h\nu]^n$ vs $h\nu$ (eV) for host CYPO matrix and from linear extrapolation of $[F(R_\infty)h\nu]^n$ to zero, we get E_g value of $Ca_9Y(PO_4)_7$ as 4.44 eV. Similarly, the E_g value of $Ca_9Y_{0.30}Tb_{0.70}(PO_4)_7$ is also determined to be 4.27 eV, which is shown in the inset of the same Fig. 7 along with its reflectance spectrum.

3.2. Photoluminescence analysis

To investigate the luminescence properties of trivalent terbium ions activated $Ca_9Y_{(1-x)}Tb_x(PO_4)_7$ (x = 0.10 – 0.90 mol) nanophosphors, photoluminescence excitation (PLE) and PL emission spectral behavior of as-synthesized series of CYPT samples are recorded. Fig. 8 corresponds to the excitation profile of crystalline $Ca_9Y_{(1-x)}Tb_x(PO_4)_7$ (x = 0.10–0.90 mol) nanophosphors which is monitored at a strong green emission wavelength i.e. 544 nm over 200–400 nm wavelength range. The entire PLE spectrum is categorized into two portions, one part is a less-intense region consisting of a broadband from 208 to 250 nm range and the second portion comprises various intense peaks that lie from 250 to 400 nm. The first group of broad excitation band arises majorly due to

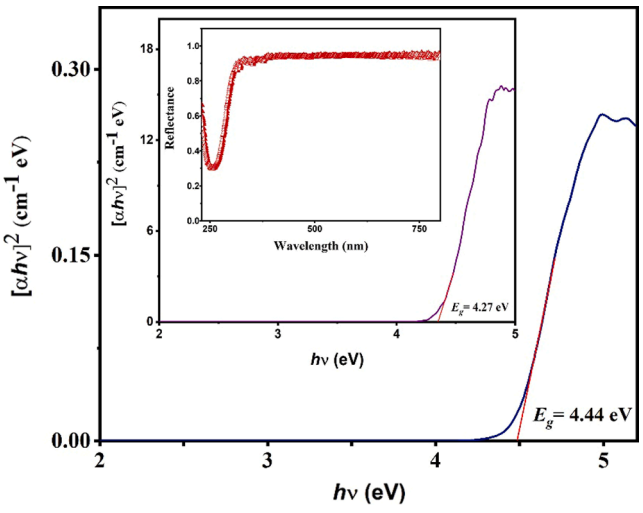

Fig. 7. A plot of $[\alpha h\nu]^2$ versus $h\nu$ for $Ca_9Y(PO_4)_7$ host sample and extrapolation to evaluate the band-gap energy employing Kubelka-Munk function. The inset shows the K-M plot and DRS of $Ca_9Y_{0.30}Tb_{0.70}(PO_4)_7$ nanophosphor system.

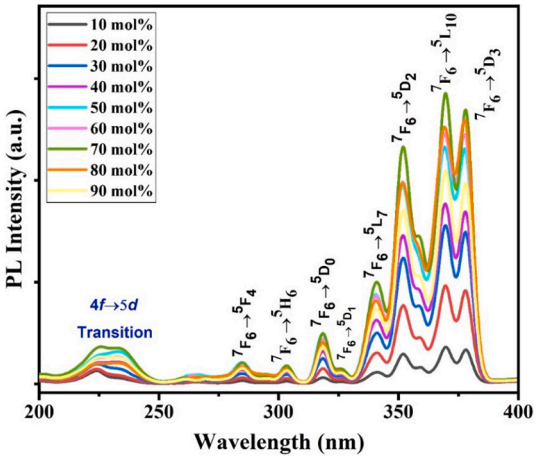

Fig. 8. The photoluminescence excitation (PLE) of $Ca_9Y_{(1-x)}Tb_x(PO_4)_7$ (x = 0.10–0.90 mol) nanophosphors (recorded at λ_{em} = 544 nm).

Laporte allowed electronic transition occurring from 4*f* to 5*d* orbitals of Tb^{3+} ion [29]. The excitation peaks corresponding to the characteristic transition of Tb^{3+} ions are centred mainly at 285 nm ($^7F_6 \rightarrow {}^5F_4$), 303 nm ($^7F_6 \rightarrow {}^5H_6$), 318 nm ($^7F_6 \rightarrow {}^5D_0$), 325 nm ($^7F_6 \rightarrow {}^5D_1$), 341 nm ($^7F_6 \rightarrow {}^5L_7$), 352 nm ($^7F_6 \rightarrow {}^5D_2$), 370 nm (most intense, $^7F_6 \rightarrow {}^5L_{10}$), and 378 nm ($^7F_6 \rightarrow {}^5D_3$) [29,34,35]. It is demonstrated from Fig. 8 that the intense intra-configurational 4*f* transitions of Tb^{3+} ion lie at high energy region (i.e. 250 – 400 nm) and they become more intense with an increase in the concentration of dopant ion. The excitable range of CYPT nanophosphors correlates well with near-Ultraviolet (NUV) or UV chips which points out their potential utility as an effective luminescence center for NUV or UV based WLEDs.

In order to further examine the PL properties of as-synthesized CYPT nanophosphors, PL emission spectra of powdered $Ca_9Y_{(1-x)}Tb_x(PO_4)_7$ (x = 0.10 – 0.90 mol) nanocrystalline samples are recorded at an excitation wavelength of 370 nm which is depicted well in Fig. 9. The spectrum is consisting of many emission peaks corresponding to characteristic emission of Tb^{3+} ion in CYPO host matrix. Basically, there are two emission states $^5D_3$ and $^5D_4$ from which emission transitions take place to different ^7F_J (J = 2 to 6) energy levels. Emission peaks situated at 415, 438, 457, and 472 nm are derived from $^5D_3$ to $^7F_5$, $^7F_4$, $^7F_3$, and $^7F_2$ transitions, respectively [19]. On other hand, four well-defined distinctive emission peaks of Tb^{3+} ion are situated at around 490 nm ($^5D_4 \rightarrow {}^7F_6$), 544 nm ($^5D_4 \rightarrow {}^7F_5$), 586 nm ($^5D_4 \rightarrow {}^7F_4$), and 621 nm ($^5D_4 \rightarrow {}^7F_3$) [6,19,36]. Out of which, emission peak at 490 nm is only electric-dipole (ED) allowed while the transitions corresponding to the remaining three emission peaks are both electric and magnetic-dipole (ED + MD) allowed [11]. The emission spectrum of $Ca_9Y_{0.30}Tb_{0.70}(PO_4)_7$ nanophosphor sample showing all the evident emission peaks and their corresponding transitions are shown in the inset of the same Fig. 9. The most intense emission peak in line with $^5D_4 \rightarrow {}^7F_5$ (544 nm) transition is turned out to be accountable for green emission of $Ca_9Y_{0.30}Tb_{0.70}(PO_4)_7$ nanophosphor.

To explain all the empirical photoluminescence phenomena like excitation and emission, a streamlined yet systematic energy level diagram is portrayed in Fig. 10. Within quantum mechanical (energy) levels of dopant Tb^{3+} ion, various radiative and non-radiative transitions take place. In the process of excitation from the lowest energy state $^7F_6$ to different levels, many higher energy states become populated which promptly relax down non-radiatively to the low lying $^5D_3$ and $^5D_4$ states to ^7F_J (J = 2–6) levels owing to the green characteristic emission of Tb^{3+} ion in CYPO host material.

It is evident from Fig. 9 that the intensity of green emission at 547 nm ($^5D_4 \rightarrow {}^7F_5$) of $Ca_9Y_{(1-x)}Tb_x(PO_4)_7$ (x = 10–90 mol%) nanophosphors is a function of concentration of Tb^{3+} ion in the phosphor system. The PL

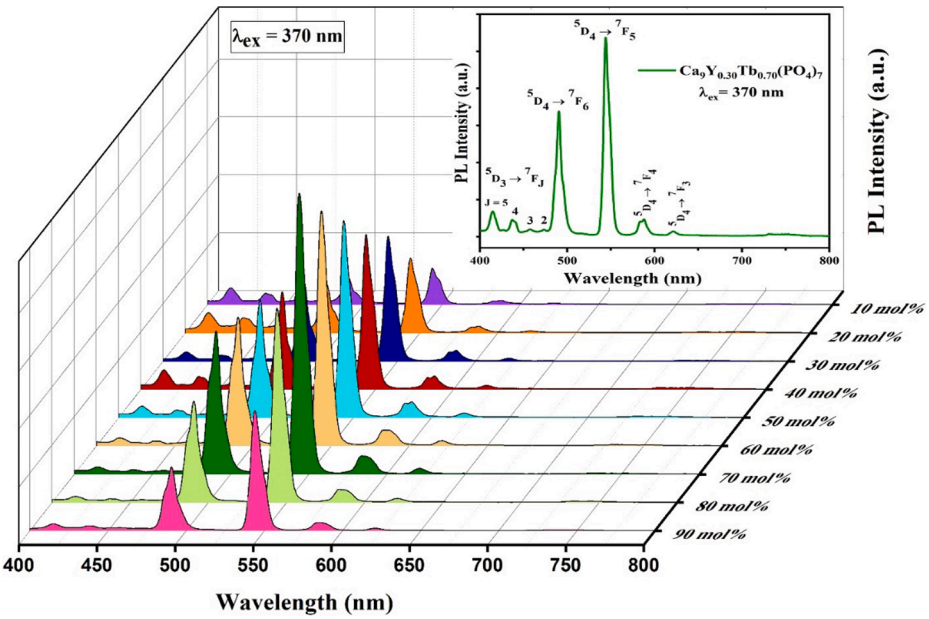

Fig. 9. PL emission spectra (at λ_{ex} = 370 nm) of the series of $Ca_9Y_{(1-x)}Tb_x(PO_4)_7$ nanophosphors (x = 0.10–0.90 mol). The inset at the top shows the PL emission spectra of $Ca_9Y_{0.30}Tb_{0.70}(PO_4)_7$ along with several possible electronic transitions.

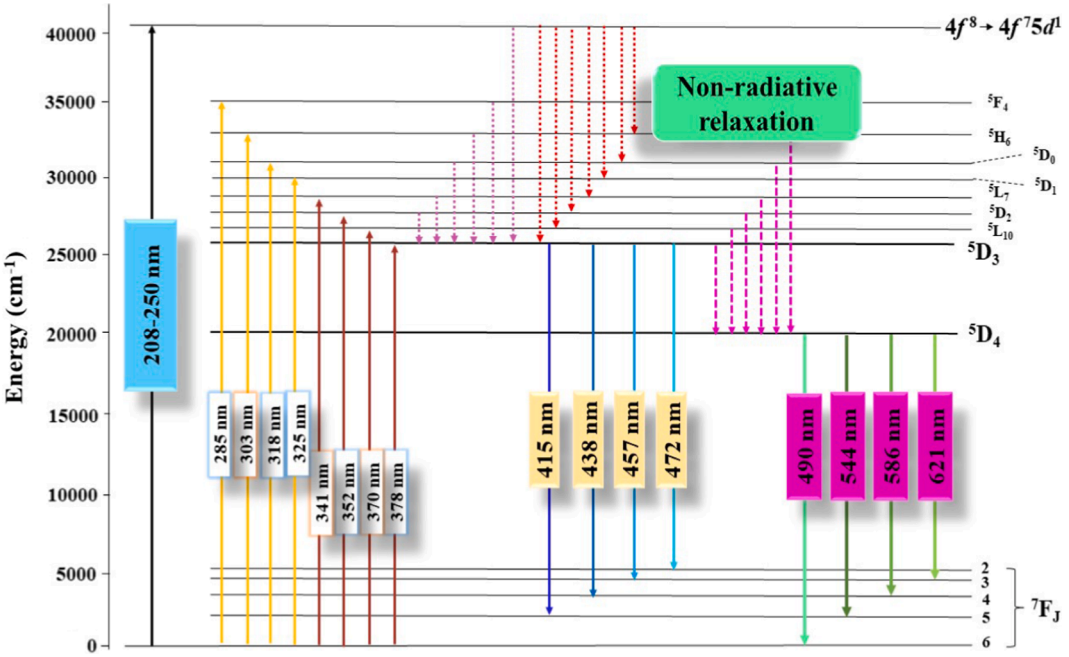

Fig. 10. A systematic energy level diagram depicting all the possible radiative and non-radiative transitions observed in Tb^{3+} doped $Ca_9Y(PO_4)_7$ nanophosphors.

emission intensity (at λ_{ex} = 370 nm) of all $^5D_4 \rightarrow {}^7F_J$ (J = 3–6) transition get increased up to 70 mol% concentration of Tb^{3+} ions and then drops down swiftly with further increase in the concentration of dopant ions. It is attributed to the occurrence of the concentration quenching phenomenon here and hence, the optimum concentration of activator Tb^{3+} ion in CYPO matrix is estimated to be 70 mol%. The concentration driven PL behavior of as-synthesized $Ca_9Y_{(1-x)}Tb_x(PO_4)_7$ (x = 10–90 mol %) nanophosphors recorded at λ_{ex} = 370 nm is elucidated clearly by Fig. 11. Getting around to concentration quenching, it is already known that the rate of non-radiative relaxation gets enhanced beyond critical concentration due to the decrease in the distance between adjacent dopant ions at higher concentration and as per Dexter's theory, three mechanisms exist corresponding to such energy transfers i.e. energy exchange interactions, re-absorptions, and electric multipolar interactions. So as to explain the exact mechanism and type of non-radiative energy transfer between adjacent Tb^{3+} ions, the critical (energy transfer) distance, R_c has to be determined by making use of Blasse's equation as given below [26,28,37]:

$$R_c = 2\left[\frac{3V}{4\pi x_c N}\right]^{1/3} \quad (6)$$

By putting experimental data obtained from crystal structure analysis of $Ca_9Y_{0.30}Tb_{0.70}(PO_4)_7$ nanophosphor as V (volume of the unit cell) = 3515.04 Å^3, N (no. of replaceable Z cations in the unit cell) = 6, and x_c (critical concentration) = 0.70 mol in the above equation, the value of R_c between neighboring dopant ions is evaluated to be around 12 Å. The

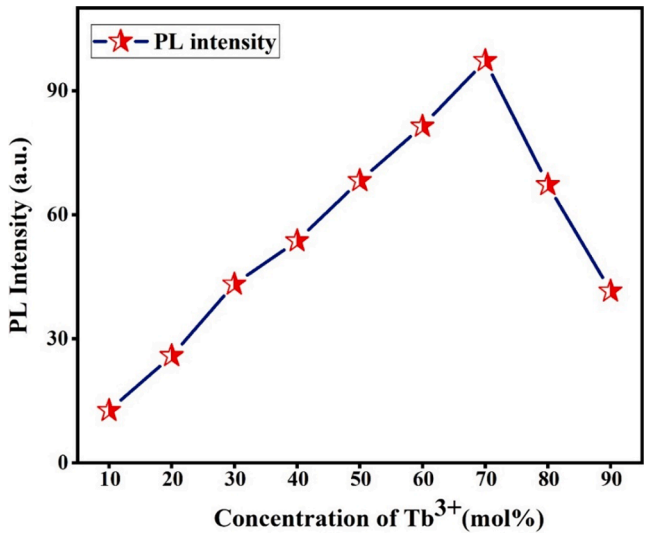

Fig. 11. Graph showing the effect of concentration of Tb^{3+} ions on PL emission intensities of $Ca_9Y_{(1-x)}Tb_x(PO_4)_7$ (x = 10–90 mol%) nanophosphors.

calculated high value (>5 Å) of R_c invalidates the probability of exchange interaction. As a matter of fact, no spectral overlap is indicated from PL investigation, hence it overrules the occurrence of radiative reabsorption mechanism to support the energy transfer process between activator Tb^{3+} ions. Consequently, it is concluded that the non-radiative decay of such energy transfer must have been directed through multipole-multipole interactions.

To determine the exact electric multipolar interaction type to support the energy transfer mechanism, a mathematical expression of Huang analysis is employed. Through this expression, Huang and co-workers submitted a relationship between PL intensity per activator ion (I/x) as a function of molar concentrations of dopant ion (x) beyond critical-emission concentration. It is described as [11,25]:

$$\log\left(\frac{I}{x}\right) = -\left(\frac{s}{d}\right)\log x + \log(f) \tag{7}$$

Here, s is the constant related to multipolar interactions, f is constant which is unaffected by the concentration of activator ion, and d signifies the dimension of the sample whose value is 3. The theoretical value of s = 6, 8, 10 represents dipole–dipole (d-d), dipole-quadrupole (d-q), and quadrupole–quadrupole (q-q) interactions, respectively. A plot of log I/x vs log x known as Huang plot is a straight-line graph giving a slope value

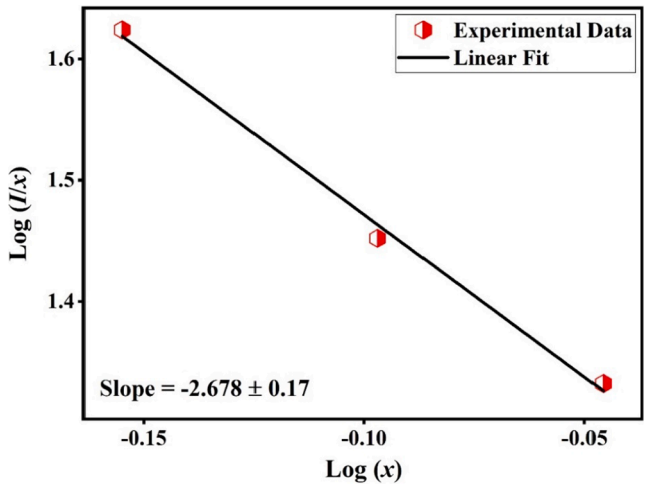

Fig. 12. Huang's Plot showing the variation of Log(I/x) with Log(x) in crystalline $Ca_9Y_{(1-x)}Tb_x(PO_4)_7$ nanophosphors (where x = 0.70, 0.80, and 0.90 mol).

of −2.678 which is represented in Fig. 12. Consequently, the value of s comes out to be 8.034 ≈ theoretical value of 8 which in turn confirms that d-q interactions are held responsible for energy transfer and concentration quenching in green-emitting Tb^{3+} ions activated CYPO nanophosphors.

To further empower energy transfer process, fluorescence lifetime values of emitting $^5D_4$ state of the complete phosphor series of $Ca_9Y_{(1-x)}Tb_x(PO_4)_7$ (x = 10 – 90 mol%) samples are recorded at λ_{ex} = 370 nm and λ_{em} = 544 nm values. The PL decay profile of CYPT nanophosphors is presented in Fig. 13 along with the fitted decay curve of $Ca_9Y_{0.30}Tb_{0.70}(PO_4)_7$ nanophosphor on a log scale which is shown in the inset of the same figure. The fitted normalized lifetime profile follows the triple-exponential fitting decay function which is given as below [17,25]:

$$I(t) = I_0 + A_1\exp\left(\frac{-t}{\tau_1}\right) + A_2\exp\left(\frac{-t}{\tau_2}\right) + A_3\exp\left(\frac{-t}{\tau_3}\right) \tag{8}$$

Here, $I(t)$ and I_0 are PL intensity at time t and 0 respectively. A_1, A_2, and A_3 signifies some constant of interactions, τ_1, τ_2, $\tau_3$corresponds to the radiative decay lifetime values for emission. Hence, for $Ca_9Y_{(1-x)}Tb_x(PO_4)_7$ (x = 10–90 mol%) nanophosphors, the average or observed lifetime values (τ_{avg} or τ_o in ms) can be evaluated under triple-exponential decay function by following equation [17]

$$\tau_{avg} = \frac{A_1\tau_1^2 + A_2\tau_2^2 + A_3\tau_3^2}{A_1\tau_1 + A_2\tau_2 + A_3\tau_3} \tag{9}$$

The as-obtained values of τ_o (in ms) for $Ca_9Y_{(1-x)}Tb_x(PO_4)_7$ (x = 0.10–0.90 mol) nanophosphors show a gradual decline from 2.287 to 2.210 ms with an increase in the concentration of Tb^{3+} ion from 10 mol % to 90 mol% which is pertaining to the fast energy transfer via non-radiative decay process. The occurrence of three non-centrosymmetric luminescence sites was depicted well from Rietveld crystal structure analysis which is accountable for a triple exponential decay in the CYPT nanophosphors system [17].

Additionally, the relevancy of fluorescence decay of low lying $^5D_4$ emitting state of Tb^{3+} ions with its varying concentration is assessed by utilizing Auzel's fitting function which is represented by the following expression [38,39]:

$$\tau(c) = \frac{\tau_R}{1 + \left(\frac{c}{c_0}\right)e^{-N/3}} \tag{10}$$

In this formula, τ(c) is the decay time at c concentration, τ_R indicates

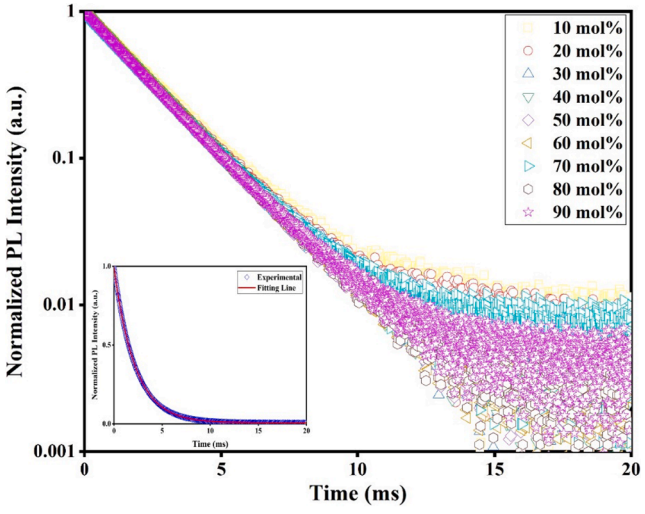

Fig. 13. The luminescence decay profile of $Ca_9Y_{(1-x)}Tb_x(PO_4)_7$ (x = 0.10–0.90 mol) nanophosphor samples for the emission from $^5D_4$ state. The inset is showing the fitted decay curve of $Ca_9Y_{0.30}Tb_{0.70}(PO_4)_7$ nanophosphor sample.

the radiative lifetime of the $^5D_4$ state, C_o is a constant and N signifies the number of phonons produced. Fig. 14 demonstrates the well fitted experimental data of PL lifetimes of CYPT nanophosphors samples that give a value of $N = 15.58$ and τ_R for emitting state of Tb^{3+} ion is also determined to be 2.315 ms. The as-obtained exact value of intrinsic radiative lifetime is further utilized to calculate non-radiative rates (A_{nR} in s^{-1}) and calculated quantum efficiency, QE (η in %) of all the samples of $Ca_9Y_{(1-x)}Tb_x(PO_4)_7$ (x = 0.10–0.90 mol) series of nanophosphors by means of following equations [23,38,39]:

$$\frac{1}{\tau_o} - \frac{1}{\tau_R} = A_{nR} \tag{11}$$

and

$$\eta = \frac{\tau_o}{\tau_R} = \frac{A_R}{A_R + A_{nR}} \tag{12}$$

Table 4 depicts a system record of calculated values of τ_o (average lifetime), NR (non-radiative rates), η (% theoretically determined QE) for varying dopant ion concentration in $Ca_9Y_{(1-x)}Tb_x(PO_4)_7$ (x = 0.10–0.90 mol) nanophosphors.

Moreover, the emission profile of CYPT nanophosphors is also serving a purpose to determine the proper emission color of the samples. The PL emission data of CYPT nanocrystalline phosphors are examined by applying the CIE1931 color co-ordinate diagram in MATLAB software. The color co-ordinates (x, y) of $Ca_9Y_{(1-x)}Tb_x(PO_4)_7$ (x = 0.10–0.90 mol) nanophosphors are outlined in Table 5 and chromaticity co-ordinates (x,y) of nanophosphor sample for the best mol% composition i.e. $Ca_9Y_{0.30}Tb_{0.70}(PO_4)_7$ indicating green emission color is portrayed in CIE1931 diagram using black dot in Fig. 15. All these structural and photoluminescent investigations support the scope and application of green-emitting $Ca_9Y_{0.30}Tb_{0.70}(PO_4)_7$ nanophosphor for various lighting and display devices.

4. Conclusion

In a nutshell, we have reported the solution combustion synthesis of green-emitting $Ca_9Y_{(1-x)}Tb_x(PO_4)_7$ (x = 0.10–0.90 mol) series of nanocrystalline phosphors for the first time. Rietveld analysis and crystal structure investigation of $Ca_9Y_{0.30}Tb_{0.70}(PO_4)_7$ nanophosphor revealed the presence of trigonal crystalline form with R3c(1 6 1) space group symmetry. Scherrer's equation and W-H plots were employed to determine the average crystal size of the series of $Ca_9Y_{(1-x)}Tb_x(PO_4)_7$ (x = 0.10–0.90 mol) nanophosphor samples whose results were further confirmed by the TEM report. The energy band-gap values of $Ca_9Y(PO_4)_7$ and $Ca_9Y_{0.30}Tb_{0.70}(PO_4)_7$ were analyzed from diffuse reflectance spectroscopy and were estimated to be 4.44 and 4.27 eV, respectively. The detailed examination of photoluminescence properties and energy-transfer mechanism (dipole-quadrupole interactions) accountable for the concentration quenching episode was thoroughly discussed. Auzel's fitting function was used to determine the radiative lifetime (2.315 ms) and thus, non-radiative transition rates from $^5D_4$ emission state of Tb^{3+} ion for all the samples of $Ca_9Y_{(1-x)}Tb_x(PO_4)_7$ (x = 0.10–0.90 mol) series were evaluated. The as-determined quantum efficiency (95.6%) and CIE

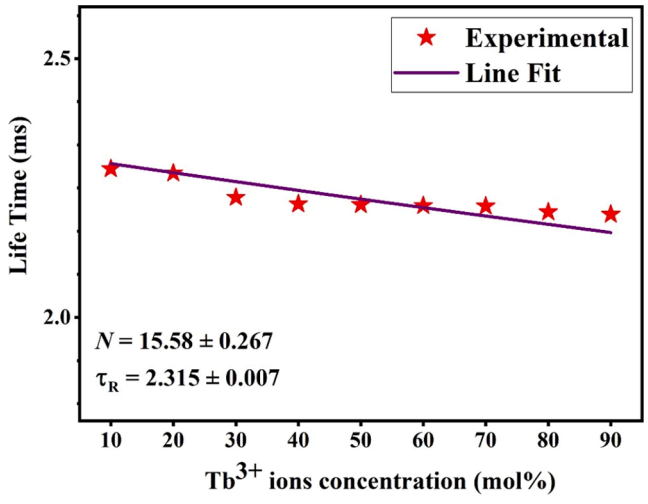

Fig. 14. Variation of decay time value(ms) of $^5D_4$ state with different concentration of dopant Tb^{3+} ions using Auzel's fitting function.

Table 4
The lifetime decay values, non-radiative relaxation rates and quantum efficiencies of $^5D_4$ emitting state in $Ca_9Y_{(1-x)}Tb_x(PO_4)_7$ (x = 0.10–0.90 mol) nanophosphors.

S. No.	Tb^{3+} concentrations (mol%)	Average lifetime (ms)	Non-radiative rates (s^{-1})	Calculated Quantum efficiency (%)
1	10	2.287	5.29	98.8
2	20	2.278	6.83	98.4
3	30	2.237	15.06	96.6
4	40	2.228	16.86	96.2
5	50	2.226	17.27	96.1
6	60	2.217	19.09	95.7
7	70	2.214	19.70	95.6
8	80	2.204	21.76	95.2
9	90	2.199	22.79	94.9

Table 5
CIE1931 color co-ordinates (x, y) for $Ca_9Y_{(1-x)}Tb_x(PO_4)_7$ (x = 0.10–0.90 mol) nanophosphors.

S. No.	Tb^{3+} concentrations (mol%)	CIE Color co-ordinates (x, y)
1	10	(0.232, 0.343)
2	20	(0.226, 0.379)
3	30	(0.248, 0.522)
4	40	(0.245, 0.486)
5	50	(0.250, 0.529)
6	60	(0.251, 0.552)
7	70	(0.252, 0.564)
8	80	(0.252, 0.559)
9	90	(0.246, 0.521)

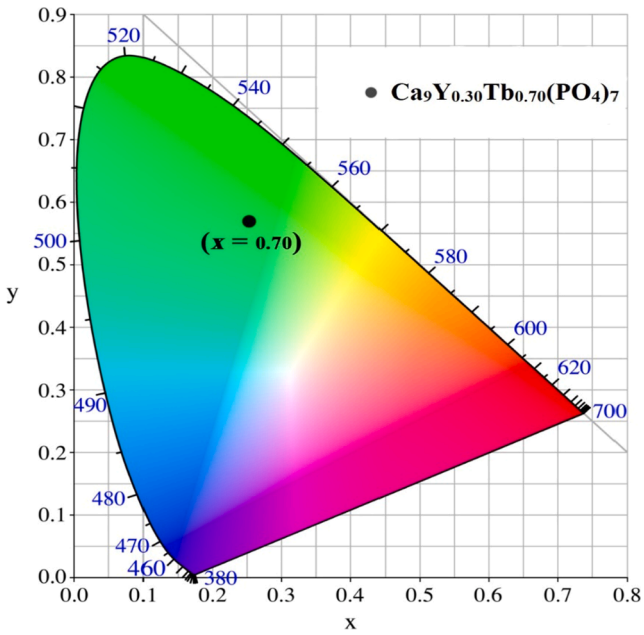

Fig. 15. CIE1931 chromaticity diagram of $Ca_9Y_{0.30}Tb_{0.70}(PO_4)_7$ nanophosphor.

co-ordinates (0.252, 0.564) of $Ca_9Y_{0.30}Tb_{0.70}(PO_4)_7$ nanophosphor indicate its potential utility in lighting sources.

Declaration of Competing Interest

The authors declare that they have no known competing financial interests or personal relationships that could have appeared to influence the work reported in this paper.

References

[1] R.V. Yadav, R.S. Yadav, A. Bahadur, S.B. Rai, Down shifting and quantum cutting from Eu^{3+}, Yb^{3+} co-doped $Ca_{12}Al_{14}O_{33}$ phosphor: a dual mode emitting material, RSC Adv. 6 (2016) 9049–9056.

[2] J. Dalal, M. Dalal, S. Devi, A. Hooda, A. Khatkar, R.K. Malik, V.B. Taxak, S. P. Khatkar, Magnetic- and electric-dipole radiative rates in multifunctional $Ba_5Zn_4Y_8O_{21}:Tb^{3+}$ nanorods, J. Mater. Sci. Mater. Electron. 30 (2019) 17547–17558.

[3] J. Huang, S. Yi, Y. Deng, W. Zhao, J. Xian, Synthesis and Luminescence Studies of Sm^{3+} Doped $Ca_9Y(PO_4)_7$ Orange-Red-Emitting Phosphor, J. Nanosci. Nanotechnol. 16 (2016) 3695–3699.

[4] X. Huang, S. Wang, B. Li, Q. Sun, H. Guo, High-brightness and high-color purity red-emitting $Ca_3Lu(AlO)_3(BO_3)_4:Eu^{3+}$ phosphors with internal quantum efficiency close to unity for near-ultraviolet-based white-light-emitting diodes, Opt. Lett. 43 (2018) 1307–1310.

[5] H. Dahiya, M. Dalal, A. Siwach, M. Dahiya, D. Kumar, Cool white light emitting $Ba_5Zn_4Y_8O2_{21}:Dy^{3+}$ nanophosphors for single-phased WLEDs, J. Mater. Sci. Mater. Electron. 29 (2018) 20750–20758.

[6] G.-G. Wang, X.-F. Wang, L.-W. Dong, Q. Yang, Synthesis and photoluminescence of green-emitting Ce^{3+}, $T^{b3}+$ co-doped $A_i6S_i2_{O13}$ phosphors with high thermal stability for white LEDs, RSC Adv. 6 (2016) 42770–42777.

[7] X. Zhang, L. Zhou, Q. Pang, M. Gong, Synthesis, photoluminescence and Judd-Ofelt analysis of red $LiGd_5P_2O_{13}$: Eu^{3+} phosphors for white LEDs, RSC Adv. 5 (2015) 54622–54628.

[8] X. Zhang, L. Zhou, M. Gong, High-brightness Eu^{3+} -doped $Ca_3(PO_4)_2$ red phosphor for NUV light-emitting diodes application, Opt. Mater. 35 (2013) 993–997.

[9] H. Guo, L. Sun, J. Liang, B. Li, X. Huang, High-efficiency and thermal-stable Eu^{3+}-activated $Ca_3Y(AlO)_3(BO_3)_4$ red-emitting phosphors for near-UV-excited white LEDs, J. Lumin. 205 (2019) 115–121.

[10] Y. Hua, D. Zhang, H. Ma, D. Deng, S. Xu, Synthesis, luminescence properties and electronic structure of Tb^{3+} -doped $Y_{(4-x)}SiAlO_8N:xTb^{3+}$ – a novel green phosphor with high thermal stability for white LEDs, RSC Adv. 6 (2016) 113249–113259.

[11] J. Dalal, A. Khatkar, M. Dalal, V.B. Taxak, S.P. Khatkar, Characteristics of down conversion green emitting $Ba_3Bi_2(PO_4)_4:Tb^{3+}$ nanosized particles for advanced illuminating devices, J. Mater. Sci. Mater. Electron. 31 (2019) 1216–1226.

[12] H. Dahiya, M. Dalal, A. Siwach, J. Dalal, V.B. Taxak, S.P. Khatkar, D. Kumar, A blue to green tunable $Ba_3GdP_3O_{12}:Tb^{3+}$ nanophosphor: structural and opto-electronic analysis, J. Mater. Sci. Mater. Electron. (2019), https://doi.org/10.1007/s10854-019-02009-1.

[13] Z.W. Zhang, L. Liu, R. Liu, X.Y. Zhang, X.G. Peng, C.H. Wang, D.J. Wang, High-brightness Eu^{3+} -doped $Ca_9Gd(PO_4)_7$ red phosphor for NUV light-emitting diodes application, Mater. Lett. 167 (2016) 250–253.

[14] H. Zhang, X. Yu, H. Sun, X. Mi, H. Zhou, X. Zhang, Z. Bai, Hydrothermal preparation and luminescence properties of $Ca_9Y(PO_4)_7:Eu^{2+}$, Mn^{2+} nanocrystals, J. Cryst. Growth 522 (2019) 61–67.

[15] X. Wua, Y. Lianga, R. Chen, M. Liu, Z. Cheng, Photoluminescence properties of emission-tunable $Ca_9Y(PO_4)_7:Tm^{3+}$, Dy^{3+} phosphor for white light emitting diodes, Mater. Chem. Phys. 129 (2011) 1058–1062.

[16] J. Dalal, S. Devi, A. Hooda, A. Khatkar, V.B. Taxak, S.P. Khatkar, Radiative and non-radiative chaacteristics of $Ca_9Bi(PO_4)_7:Eu^{3+}$ nano-phosphor for solid state lighting devices, J. Lumin. 216 (2019).

[17] H. Dahiya, M. Dalal, A. Singh, A. Siwach, M. Dahiya, S. Nain, V.B. Taxak, S. P. Khatkar, D. Kumar, Spectroscopic characteristics of Eu^{3+}-activated $Ca_9Y(PO_4)_7$ nanophosphors in Judd-Ofelt framework, Solid State Sci. (2020), https://doi.org/10.1016/j.solidstatesciences.2020.106341.

[18] C.H. Huang, T.M. Chen, W.R. Liu, Y.C. Chiu, Y.T. Yeh, S.M. Jang, A Single-Phased Emission-Tunable Phosphor $Ca_9Y(PO_4)_7:Eu^{2+}$, $M^{n2}+$ with Efficient Energy Transfer for White-Light-Emitting Diodes, ACS Appl. Mater. Interfaces 2 (2010) 259–264.

[19] M. Tang, Y. Fan, Z. Qiu, J. Zhang, L. Yu, C. Li, S. Lian, W. Zhou, Preparation, luminescence properties and energy transfer of $Ca_9Y(PO_4)_7$: Eu^{2+}-Tb^{3+} phosphors, J. Am. Ceram. Soc. 100 (2017) 2991–2996.

[20] S. Du, D. Wang, Y. Wang, S. Xin, Q. Qiang, X. Ma, Synthesis and up-conversion luminescence of Yb^{3+} /Er^{3+} /Tm^{3+} doped $Ca_9Y(PO_4)_7$, New J. Chem. (2015), https://doi.org/10.1039/C5NJ00913H.

[21] J. Sun, W. Zhou, Y. Sun, J. Zeng, Broadband near-infrared downconversion luminescence in Eu^{2+}–Yb^{3+} codoped $Ca_9Y(PO_4)_7$, Opt. Commun. 296 (2013) 84–86.

[22] C.H. Huang, T.W. Kuo, T.M. Chen, Novel red-emitting phosphor $Ca_9Y(PO_4)_7:Ce^{3+}$, $M^{n2}+$ with energy transfer for fluorescent lamp application, ACS Appl. Mater. Interfaces 2 (2010) 1395–1399.

[23] M. Dalal, J. Dalal, S. Chahar, H. Dahiya, S. Devi, P. Dhankhar, S. Kumar, V. B. Taxak, D. Kumar, S.P. Khatkar, A hybrid treatment of $Ba_2LaV_3O_{11}:Eu^{3+}$ nanophosphor system: First-principal and experimental investigations into electronic, crystal and the optical structure, J. Alloys Compd. 805 (2019) 84–96.

[24] J. Zhong, D. Chen, Y. Zhou, Z. Wan, M. Ding, W. Bai, Z. Ji, New Eu^{3+}-activated perovskite $La_{(0.5)}Na_{(0.5)}TiO3$ phosphors in glass for warm white light emitting diodes, Dalton Trans. 45 (2016) 4762–4770.

[25] A. Siwach, M. Dahiya, M. Dalal, D. Kumar, $Ca_9Gd(PO_4)_7:Sm^{3+}$ -a novel single-phased down converting orange-red-emitting nanophosphor, J. Mater. Sci. Mater. Electron. (2020), https://doi.org/10.1007/s10854-020-03940-4.

[26] A. Hooda, S.P. Khatkar, A. Khatkar, R.K. Malik, J. Dalal, S. Devi, V.B. Taxak, Crystal structure, synthesis and photoluminescent properties of a reddish-orange light emitting $SrGdAlO_4$: Sm^{3+} nanophosphor, Mater. Chem. Phys. 232 (2019) 39–48.

[27] S. Devi, V.B. Taxak, S. Chahar, M. Dalal, J. Dalal, A. Hooda, A. Khatkar, R.K. Malik, S.P. Khatkar, Crystal chemistry and optical analysis of a novel perovskite type $SrLa_2Al_2O_7:Sm^{3+}$ nanophosphor for white LEDs, Ceram. Int. 45 (2019) 15571–15579.

[28] H. Dahiya, M. Dalal, J. Dalal, V.B. Taxak, S.P. Khatkar, D. Kumar, Synthesis and luminescent properties of Tb^{3+} doped $BaLa_2ZnO_5$ nanoparticles, Mater. Res. Bull. 99 (2018) 86–92.

[29] S. Chahar, R. Devi, M. Dalal, M. Bala, J. Dalal, P. Boora, V.B. Taxak, R. Lather, S. P. Khatkar, Color tunable nanocrystalline $SrGd_2Al_2O_7:Tb^{3+}$ phosphor for solid state lighting, Ceram. Int. 45 (2019) 606–613.

[30] S. Mustapha, M.M Ndamitso, A.S Abdulkareem, J.O Tijani, D.T Shuaib, A.K Mohammed, A. Sumaila, Comparative study of crystallite size using Williamson-Hall and Debye-Scherrer plots for ZnO nanoparticles, Adv. Nat. Sci.: Nanosci. Nanotechnol. 10 (2019) 045013 (8pp).

[31] D. Nath, F. Singh, R. Das, X-ray diffraction analysis by Williamson-Hall, Halder-Wagner and size-strain plot methods of CdSe nanoparticles- a comparative study, Mater. Chem. Phys. 239 (2020) 122021.

[32] S. Devi, M. Dalal, J. Dalal, A. Hooda, A. Khatkar, V.B. Taxak, Near-ultraviolet excited down-conversion Sm^{3+} doped $Ba_5Zn_4Gd_8O_{21}$ reddish-orange emitting nano-diametric rods for white LEDs, Ceram. Int. 45 (2019) 7397–7406.

[33] Y. Liu, J. Silver, R.J. Xie, J. Zhang, H. Xu, H. Shao, J. Jiang, H. Jiang, An excellent cyan-emitting orthosilicate phosphor for NUV-pumped white LED application, J. Mater. Chem. C 5 (2017) 12365–12377.

[34] K.N. Kumar, R. Padma, Y.C. Ratnakaram, M. Kang, Bright green emission from f-MWCNT embedded co-doped Bi^{3+}-Tb^{3+}:polyvinyl alcohol polymer nanocomposites for photonic applications, RSC Adv. 7 (2017) 15084.

[35] J.J. Batalla, A.N. Meza-Rocha, H.G. Munoz, I. Camarillo, U. Caldino, Luminescence properties of Tb^{3+}-doped zinc phosphate glasses for green laser application, Opt. Mater. 58 (2016) 406–411.

[36] J. Zhou, Z. Xia, Multi-color emission evolution and energy transfer behavior of $La_3GaGe_5O_{16}:Tb^{3+}$, $E^{u3}+$ phosphors, J. Mater. Chem. C 2 (2014) 6978–6984.

[37] H. Xu, L. Wang, D. Qu, Z. Si, J. Shi, Structure and photoluminescence properties of novel $Sr_6Ca_4(PO_4)_6F_2$: Re (Re = $E^{u2}+$, $M^{n2}+$) phosphors with energy transfer for white-emitting LEDs, RSC Adv. 7 (2017) 41282–41288.

[38] J. Dalal, M. Dalal, S. Devi, S. Chahar, A. Hooda, A. Khatkar, R.K. Malik, V.B. Taxak, S.P. Khatkar, $Ba_5Zn_4Gd_8O_{21}:Tb^{3+}$ -Structural Characterization and the Judd-ofelt parameterization from emission spectra, Methods Appl. Fluoresc. (2019), https://doi.org/10.1088/2050-6120/ab33b6.

[39] J. Dalal, M. Dalal, S. Devi, R. Devi, A. Hooda, A. Khatkar, V.B. Taxak, S.P. Khatkar, Structural Analysis and Judd-Ofelt parameterization of $Ca_9Gd(PO_4)_7:Eu^{3+}$ Nanophosphor for Solid-State Illumination, J. Lumin. 210 (2019) 293–302.